Check for updates

Fabrication of Mo$_{1.33}$CT$_z$ (MXene)–cellulose freestanding electrodes for supercapacitor applications†

Ahmed S. Etman, [ID] * Joseph Halim [ID] and Johanna Rosen*

MXenes are two-dimensional (2D) transition metal carbides/nitrides with high potential for energy storage devices owing to their high flexibility, conductivity and specific capacitance. However, MXene films tend to suffer from diffusion limitation of ions within the film, and thus their thickness is commonly reduced to a few micrometers (mass loadings <1 mg cm^{-2}). Herein, a straightforward one-step protocol for synthesizing freestanding Mo$_{1.33}$CT$_z$–cellulose composite electrodes with high MXene loading is reported. By varying the amount of the cellulose content, a high gravimetric capacitance (up to 440 F g^{-1} for 45 wt% cellulose content, ∼5.9 μm thick film) and volumetric capacitance (up to 1178 F cm^{-3} for 5 wt% cellulose content, ∼4.8 μm thick film) is achieved. These capacitance values are superior to those for the pristine MXene film, of a similar MXene loading (1.56 mg cm^{-2}, ∼4.2 μm thick film), delivering values of about 272 F g^{-1} and 1032 F cm^{-3}. Interestingly, the Mo$_{1.33}$CT$_z$–cellulose composite electrodes display an outstanding capacitance retention (∼95%) after 30 000 cycles, which is better than those reported for other Mo$_{1.33}$CT$_z$-based electrodes. Furthermore, the presence of cellulose inside a thick composite electrode (∼26 μm, MXene loading 5.2 mg cm^{-2}) offers a novel approach for opening the structure during electrochemical cycling, with resulting high areal capacitance of about 1.4 F cm^{-2}. A symmetric device of Mo$_{1.33}$CT$_z$–cellulose electrodes featured a long lifespan of about 35 000 cycles and delivered a device capacitance up to 95 F g^{-1}. The superior performance of the Mo$_{1.33}$CT$_z$–cellulose electrodes in terms of high gravimetric, volumetric, and areal capacitances, long lifespan, and promising rate capability, paves the way for their use in energy storage devices.

1. Introduction

Two-dimensional (2D) transition metal oxides,[1–6] chalcogenides,[7,8] and carbides (MXenes)[9,10] are materials with unique physical and chemical properties compared to their bulk counterparts. MXenes have general formula of M$_{n+1}$X$_n$T$_x$ where M = transition metal (*e.g.* Ti, Mo, V, Nb, or W), X = C or N, and T = surface termination group (*e.g.* –OH, –F, –Cl, or –O).[9,11,12] They are typically prepared by selective etching of the A element (A = Al, Si or Ga)[13,14,15] from their 3D bulk precursor MAX phase. MXenes possess unique properties such as high conductivity, solution-based processability, high capacitance, flexibility and mechanical strength.[16–18] Therefore, they have attracted a lot of research interest in the last few years, and have been tested for a variety of applications including plasmonic devices,[19,20] sensors,[21] catalysis (*e.g.* H$_2$ evolution,[22–26] CO$_2$ reduction[27,28] and N$_2$ reduction[28,29] reactions),

water-treatment,[30] electrochemical actuators,[31] electromagnetic interference shielding,[32] batteries,[33–35] and supercapacitors.[36,37] The latter application of MXenes has been most investigated owing to the MXene showing a high specific capacitance (gravimetric or volumetric), a high conductivity, and an ability to form freestanding electrodes.[38] However, as the thickness of the freestanding electrodes increases, the capacitance of the MXene decreases significantly due to stacking of MXene flakes, diffusion limitations, and iR-drop (ohmic-drop).[39,40]

Cellulose is a natural sustainable material which can be extracted from a plenty of natural resources such as tree, algae, bacteria, and others.[41–43] Owing to its flexibility, mechanical strength, abundance, biodegradability, and solution processability, it has been used in many applications, including fabrication of paper electrodes[44–46] for flexible and wearable electronic devices. Recently, composite electrodes of MXenes and cellulose were synthesized and tested for applications such as inks for 3D-printed textiles,[47] wearable sensors,[21] and supercapacitors.[48,49] For example, S. Jiao *et al.* reported the use of Ti$_3$C$_2$T$_z$ MXene and bacterial cellulose in stretchable and flexible all-solid-state micro-supercapacitors.[48]

Department of Physics, Chemistry and Biology (IFM), Linköping University, SE-58183, Linköping, Sweden. E-mail: ahmed.etman@liu.se, johanna.rosen@liu.se
† Electronic supplementary information (ESI) available. See DOI: 10.1039/d0ma00922a

Also, Y. Wang *et al.* showed that the bacterial cellulose can provide tunnels between the $Ti_3C_2T_z$ flakes upon freeze-dying, which can improve the capacitance for MXene films with high mass loading.[17] Later on, W. Tian *et al.* described the use of $Ti_3C_2T_z$ MXene with cellulose nanofibers as inks for printing flexible micro-supercapacitors.[49] To date, most of the literature studies investigating MXene–cellulose composites have focused on the titanium based MXene (*e.g.* $Ti_3C_2T_z$), while other types of MXene composites such as molybdenum-based, remain to be explored.

$Mo_{1.33}CT_z$ MXene with ordered divacancies is a high capacitance MXene which was first reported in 2017.[50] The $Mo_{1.33}CT_z$ was synthesized by selective etching of Sc and Al elements from $(Mo_{2/3}Sc_{1/3})_2AlC$ *i*-MAX phase (quaternary *in-plane* ordered MAX phase) using hydrofluoric acid (HF) or a mixture of LiF/HCl.[50] The capacitance of the $Mo_{1.33}CT_z$ MXene was found to decrease, especially at high scan rates, as the electrode thickness increased, in line with typical MXene behavior.[50] Later on, L. Qin *et al.* reported that the performance of the $Mo_{1.33}CT_z$ electrodes can be improved by forming a composite material with a PEDOT:PSS polymer.[51] However, the performance was evaluated for thin electrodes with a relatively low mass loading, which may make their use in commercial devices challenging. Thus, there is a need to identify an electrode fabrication method to allow use of thick electrodes with high mass loading, while ensuring a high specific capacitance and a long lifespan of the electrodes.

In this paper, we introduce a simple, straightforward strategy for synthesizing freestanding $Mo_{1.33}CT_z$–cellulose composite electrodes. The amount of cellulose was varied between 0 and 45 wt% for electrodes with relatively low and high MXene loadings. The electrodes were tested for supercapacitor applications and displayed outstanding volumetric and gravimetric capacitances up to 1178 F cm^{-3} and 440 F g^{-1}, respectively. Furthermore, the composite electrodes showed superior long-term cycling (95% retention after 30 000 cycles) and rate capability (150 F g^{-1} at 20 A g^{-1}). Symmetric devices of $Mo_{1.33}CT_z$–cellulose composite electrodes were also demonstrated, exhibiting a capacitance up to 95 F g^{-1} and a life span over 35 000 cycles.

2. Results and discussions

The $Mo_{1.33}CT_z$–cellulose composite electrodes were prepared using a simple vacuum filtration method. Fig. 1a and b show a schematic illustration of the synthesis method. Typically, the freshly prepared $Mo_{1.33}CT_z$ aqueous suspension was mixed with a specific amount of cellulose and then sonicated for about 20–30 minutes. After vacuum filtration, flexible free-standing films of $Mo_{1.33}CT_z$–cellulose were obtained as shown in Fig. 1f. The samples were nominated according to their MXene loading and weight percentage of cellulose content. In particular, two series were fabricated, one with low MXene content (about 1.56–1.80 mg cm^{-2}) which was assigned as L-Mo_xC-% Cel; and the second series with high MXene content (about 5.20 mg cm^{-2}) which was referred to as H-Mo_xC-% Cel.

The X-ray diffraction (XRD) pattern for the $Mo_{1.33}CT_z$–cellulose composite films was similar to that of $Mo_{1.33}CT_z$ MXene, see Fig. 1c.[50] The indices of the observed peaks can be assigned as *000l* reflections of the hexagonal unit cell, as explained in details in a previous report.[51] Notably, the *0002* peak did not display a significant peak shift as compared to the pristine
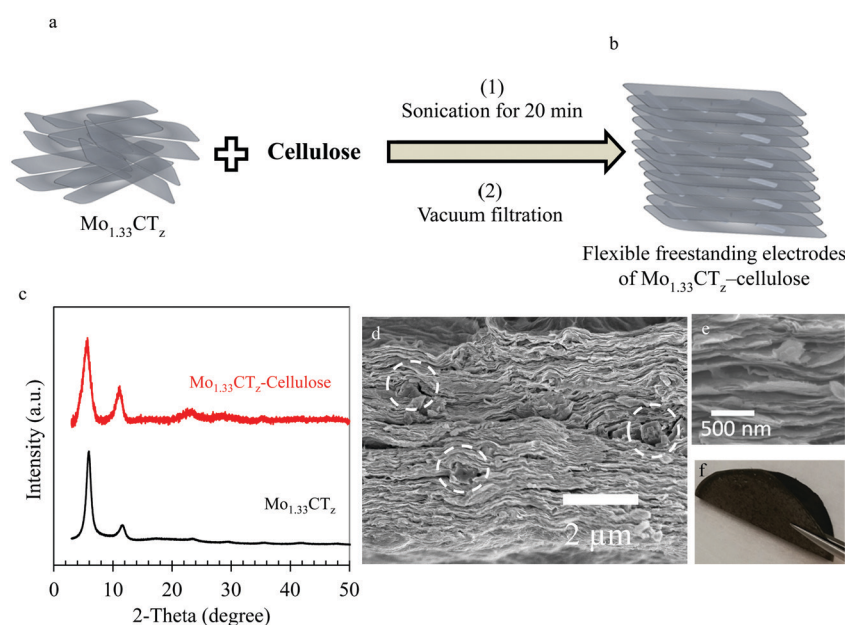

Fig. 1 Synthesis, structure, and morphology of $Mo_{1.33}CT_z$–cellulose composite film (L-Mo_xC-45% Cel): (a) and (b) show a schematic illustration of the synthesis method for the $Mo_{1.33}CT_z$–cellulose freestanding electrodes. (c) XRD patterns of the pristine (black) and $Mo_{1.33}CT_z$–cellulose composite (red). (d) and (e) Cross-section SEM images of a $Mo_{1.33}CT_z$–cellulose composite film at low and high magnification, respectively. The white circles in (d) shows cellulose imbedded between the MXene layers. (f) Photo of the freestanding $Mo_{1.33}CT_z$–cellulose film, showing its flexibility.

MXene, indicating that there was no intercalation process occurring in the MXene during the synthesis process, and thus no change in the structure of $Mo_{1.33}CT_z$. However, the peak broadening for the composite films was larger than that of the pristine MXene, which can be attributed to the different interlayer spacing between different crystals upon combination with cellulose. It worth mentioning that the structure of the pristine $Mo_{1.33}CT_z$ MXene was explored earlier using HRTEM and SAED.[50] Although the pristine cellulose possesses relatively large crystal size up to tenths of micrometers (see Fig. S1a, ESI†), it is, however, degraded into a much smaller crystals upon treatment with a base such as NaOH or tetra-butyl ammonium hydroxide (TBAOH).[52–56] For instance, when the cellulose in the present study was treated with TBAOH, the size of the cellulose crystals decreased significantly, down to well below one micrometer, in agreement with previous reports (see Fig. S1b and c, ESI†).[52–56] Likewise, when the cellulose was mixed and sonicated with the MXene suspension, the cellulose crystal degraded into small parts imbedded between the MXene layers, as shown with the white circles in Fig. 1d. This cellulose degradation is explained by dissolution caused by the TBAOH present in the MXene suspension. Scanning electron microscopy showed that the morphology of the $Mo_{1.33}CT_z$–cellulose composite film was similar to the pristine $Mo_{1.33}CT_z$, shown in Fig. S2a (ESI†), having a typical layered structure (see Fig. 1d and e). Furthermore, the thickness of L-Mo_xC-25% Cel film was about 4.8 μm which is very close to the thickness of L-Mo_xC-0% Cel film of about 4.2 μm (see Fig. S2a and c, ESI†). This indicates that the addition of cellulose does not cause a drastic increase in the volume of the $Mo_{1.33}CT_z$ film. On the other hand, the microstructure of the composite films is different than that of the pristine MXene, as the cellulose content increases the restacking of the MXene layers decreases due to the presence of the cellulose between the layers (see Fig. 2d and Fig. S2a–c, ESI†).

The $Mo_{1.33}CT_z$–cellulose composite films were tested as freestanding electrodes for supercapacitors using cyclic voltammetry (CV) and constant current techniques. Preliminary experiments were performed to screen the optimum potential window for cycling our electrodes in 1 M H_2SO_4 electrolyte solution (see Fig. S3, ESI†). The results showed that the best performance can be achieved between −0.3 to 0.3 V vs. Ag/AgCl (3.5 M KCl). Some previous reports on $Mo_{1.33}CT_z$ MXene used a lower cut-off potential of −0.35 V;[50,51] however, we found for our electrodes the best coulombic efficiency and long-term cycling can be achieved when the lower cut-off is limited to −0.3 V. Fig. 2a–c display a comparison between the electrochemical performance for the electrodes with (L-Mo_xC-25% Cel) and without (L-Mo_xC-0% Cel) cellulose, keeping the MXene loading almost the same of about 1.56 mg cm^{-2}. As can be seen in Fig. 2a and b, a pseudocapacitive behavior[57] was observed for both samples, and the cyclic voltammogram shape did not change much upon inclusion of cellulose between the $Mo_{1.33}CT_z$ MXene nanosheets. However, the magnitude of the normalized current in the presence of cellulose (i.e. for L-Mo_xC-25% Cel) is higher than that of the $Mo_{1.33}CT_z$ MXene (i.e. L-Mo_xC-0% Cel),

indicating that the cellulose provides more tunnels between the $Mo_{1.33}CT_z$ layers, resulting in an increase of the interfacial surface accessed by the electrolyte ions (H$^+$) and hence an increase in the available capacitance.[17] As can be seen from the Nyquist plots (see Fig. 2g and h), the intersection points on the real axis which reflect the internal resistance of the electrodes, are located almost at the same position for the pristine MXene and the $Mo_{1.33}CT_z$–cellulose composite electrodes. Furthermore, the charge transfer resistance (R_{ct}) which is reflected by the diameter of semicircle on the Nyquist plots, decreases upon adding the cellulose to the MXene electrodes.

Likewise, the galvanostatic measurements (see Fig. 2c) showed a similar trend as that of the CVs experiments. At low applied current density of about 1 A g^{-1}, the cellulose containing electrodes featured a specific capacitance of about 327 F g^{-1} which was higher than that of $Mo_{1.33}CT_z$ MXene of about 230 F g^{-1}. Similarly, at high applied current density of about 10 A g^{-1}, the cellulose containing electrodes delivered a specific capacitance of about 100 F g^{-1}, whereas the $Mo_{1.33}CT_z$ MXene specific capacitance was only about 40 F g^{-1}. The decrease in specific capacitance at high rates can be attributed to a combination of diffusion limitations and an increased iR drop.[58] Interestingly, the rate performance of the L-Mo_xC-25% Cel can be improved by using 3 M H_2SO_4 electrolyte rather than 1 M H_2SO_4, (see Fig. 2d).[17,49] For instance, when the applied current density was raised by two orders of magnitude (from 0.5 to 50 A g^{-1}) the capacitance retention was about 22% in 3 M H_2SO_4 and 6% in 1 M H_2SO_4. This enhancement of the rate capability can be attributed to the increase in ionic conductivity of the electrolyte.[32]

The electrode mass loadings and dimensions are important parameters which can influence the electrode performance.[57,59] When we compared the electrochemical performance for L-Mo_xC-25% Cel electrodes possessing different diameters and hence mass loadings, the results showed that the specific capacitance of the electrode with larger diameter (6.4 mm, mass loading 465 μg) deviated from that of the smaller diameter (4 mm, mass loading 180 μg) at high rate (see Fig. S4, ESI†). This can be attributed to the increased iR-drop effect for the electrode with the larger diameter.[58,59] Therefore, care has to be taken when comparing different electrode performance. Many literature reports, however, compare the normalized capacitance (specific capacitance) values while ignoring the absolute electrode mass and the dimensions, which significantly affect the electrode performance.

The effect of cellulose content on the accessible capacitance of the $Mo_{1.33}CT_z$–cellulose composite electrodes was exploited by comparing the performance of electrodes with variable cellulose content, but similar MXene loadings (1.56–1.80 mg cm^{-2}). Fig. 2e and f display the variation of the gravimetric specific capacitance as a function of scan rates and current densities, respectively, for L-Mo_xC-45% Cel, L-Mo_xC-25% Cel, L-Mo_xC-5% Cel, and L-Mo_xC-0% Cel electrodes with cellulose contents of about 45, 25, 5 and 0 wt%, respectively. As a general trend, the accessible specific capacitance increases as the cellulose content increases. Sample L-Mo_xC-45% Cel showed the best performance in terms of accessible specific capacitance at
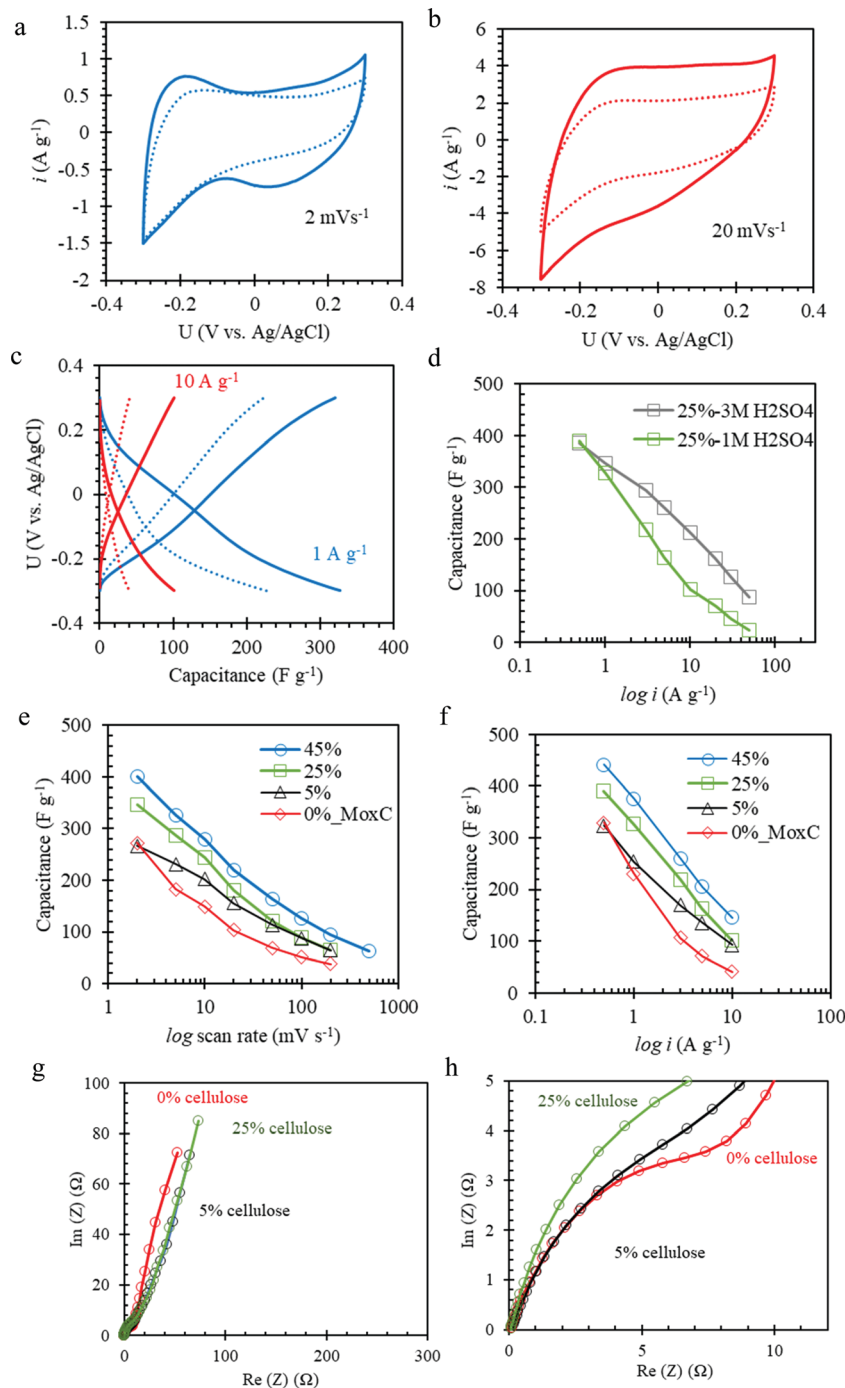
Fig. 2 Electrochemical performance of thin electrodes of $Mo_{1.33}CT_z$–cellulose composite with relatively low MXene loadings (1.5–1.8 mg cm^{-2}): (a) and (b) cyclic voltammogram of L-Mo$_x$C-25% Cel (solid lines) and L-Mo$_x$C-0% Cel (dotted lines) electrodes at scan rates of 2 and 20 mV s^{-1}, respectively. (c) Potential capacitance profiles for L-Mo$_x$C-25% Cel (solid line) and L-Mo$_x$C-0% Cel (dotted line) electrodes at applied current densities of 1 (blue lines) and 10 (red lines) A g^{-1}. (d) Variation of the discharge capacitances with applied current densities for L-Mo$_x$C-25% Cel electrodes in 1 M (green squares) and 3 M (grey squares) H$_2$SO$_4$ electrolyte solutions. (e) and (f) Variation of the discharge capacitances with scan rates and applied current densities, respectively, for electrodes with cellulose content of 0% (red diamonds), 5% (black triangles), 25% (green squares), and 45% (blue circles). (g) and (h) Nyquist plots of the L-Mo$_x$C-0% Cel (red), L-Mo$_x$C-5% Cel (black), L-Mo$_x$C-25% Cel (green) electrodes.

different rates (see Table S1, ESI†). However, this sample contains about 45 wt% dead-weight (*i.e.* cellulose) which in terms of gravimetric capacitance considering overall electrode mass is of impractical use. For example, when we compare the gravimetric capacitance of the electrodes normalized to the

overall electrode mass including the cellulose (see Fig. S3, ESI†), we find that the capacitance of L-Mo$_x$C-25% Cel is higher than both L-Mo$_x$C-45% Cel and L-Mo$_x$C-0% Cel. Therefore, the electrodes with cellulose content about 25 wt% (L-Mo$_x$C-25% Cel) are more practical from gravimetric point of view. For the

areal and volumetric capacitances, as a general trend, the electrodes containing cellulose behave superior to those without the cellulose (see Fig. S3 and Table S1, ESI†), however, in the discussion below we are focusing on the variation of the gravimetric specific capacitance of the electrodes.

The long-term cycling of the L-Mo$_x$C-25% Cel electrodes in 1 M H$_2$SO$_4$ solution showed outstanding long-term cycling over 30 000 cycles at current densities ranging from 3 to 50 A g^{-1}, see Fig. 3a and b. Notably, at an applied current density of about 20 A g^{-1}, the electrodes delivered a capacitance of about 65 F g^{-1} over 30 000 cycles with capacitance retention of about 95% and coulombic efficiency of about 99.5% after the first few cycles. The morphology and structure of the electrodes was maintained after the long-term cycling (see Fig. S5a, ESI†). The minor reduction in capacitance during electrochemical cycling can be attributed to dissolution of Mo$_{1.33}$CT$_z$ in the electrolyte.[50,51] Interestingly, the accessible capacitance of the L-Mo$_x$C-25% Cel electrodes in 3 M H$_2$SO$_4$ was raised to about 150 F g^{-1} at applied current density of about 20 A g^{-1}, see Fig. 3c. However, the capacitance retention was lowered to about 88% after 30 000 cycles implying that the dissolution in the 3 M H$_2$SO$_4$ is more pronounced. Previous literature reports on Mo$_{1.33}$CT$_z$ showed a capacitance retention of about 84% after 10 000 cycles at 10 A g^{-1} (see Table S2, ESI†).[50,51] The promising lifespan of L-Mo$_x$C-25% Cel electrodes can be attributed to the presence of cellulose inside the electrodes which improves the flexibility and reduces the internal strain during the long-term cycling.[45] This is further supported by the demonstrated long-term cycling of L-Mo$_x$C-0% Cel electrodes (pristine MXene), where Fig. 3d shows that the

electrodes performed well for about 5000 cycles, after which the coulombic efficiency dropped significantly, indicating that side reactions become more pronounced.

For practical application of Mo$_{1.33}$CT$_z$–cellulose composite electrodes in energy storage devices, the MXene loading needs to be raised and the cellulose content has to be decreased owing to its poor conductivity and negligible electrochemical contribution. With this in mind, we successfully prepared electrodes with 5 wt% cellulose content and MXene loading of about 5.2 mg cm^{-2}, which is 3 times higher than the loading of the L-Mo$_x$C-% Cel series. These electrodes were denoted H-Mo$_x$C-5% Cel. The SEM cross-section shows that the electrode thickness is about 26 μm, see Fig. 4b. Interestingly, at higher magnification it can be seen that the layered morphology of the Mo$_{1.33}$CT$_z$ MXene is maintained eventhough increasing the thickness by a factor of 5 as compared to the L-Mo$_x$C-% Cel series.

The CVs of H-Mo$_x$C-5% Cel electrodes at scan rate of 10 mV s^{-1} displayed an increase in the accessible capacitance upon cycling, see Fig. 4a. For instance, the first scan delivered a capacitance of about 133 F g^{-1}, whereas the 30th scan capacitance was about 160 F g^{-1}, see inset in Fig. 4a. This observation indicates that the structure was opened during electrochemical cycling and that the interfacial surface area accessed by the electrolyte was increased. It should be noted that when the thick electrodes were fabricated without cellulose (*i.e.* Mo$_{1.33}$CT$_z$ MXene only), they did not show the corresponding behavior of opening the strucutre by electrochemical cycling (see Fig. S6, ESI†). The latter result emphasize the role played by the presence of cellulose crystals in opening the strucutre of the thick electrodes. Electrochemical
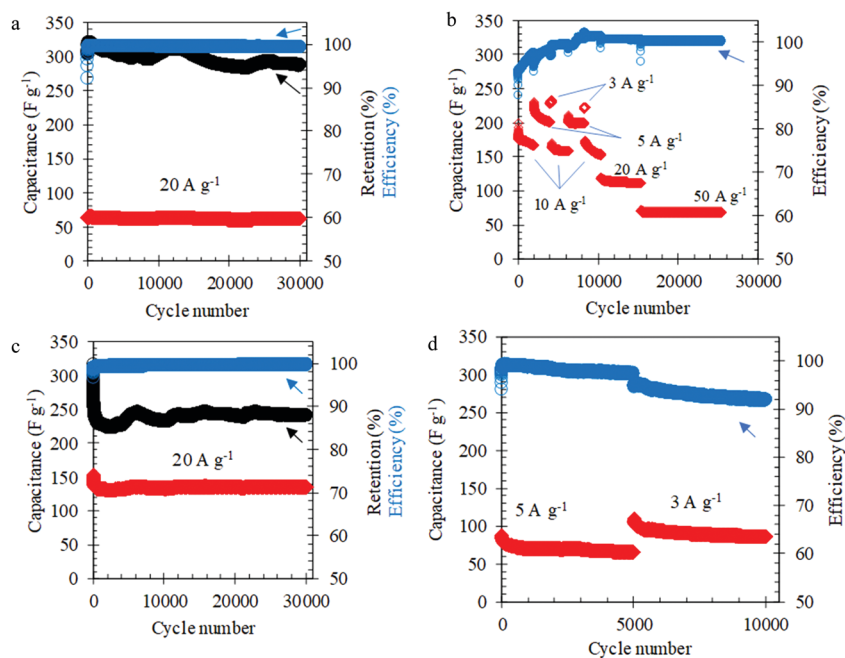

Fig. 3 Long-term cycling of thin electrodes of Mo$_{1.33}$CT$_z$–cellulose composite with relatively low MXene loadings (1.5–1.8 mg cm^{-2}): (a) and (b) variation of discharge capacitance with cycle number for L-Mo$_x$C-25% Cel electrodes in 1 M H$_2$SO$_4$ solution under constant applied current density of 20 A g^{-1} and different applied current densities, respectively. (c) Variation of discharge capacitance with cycle number for L-Mo$_x$C-25% Cel electrodes in 3 M H$_2$SO$_4$ solution under constant applied current density of 20 A g^{-1}. (d) Variation of discharge capacitance with cycle number for L-Mo$_x$C-0% Cel electrodes in 1 M H$_2$SO$_4$ solution at different applied current densities of 3 and 5 A g^{-1}.
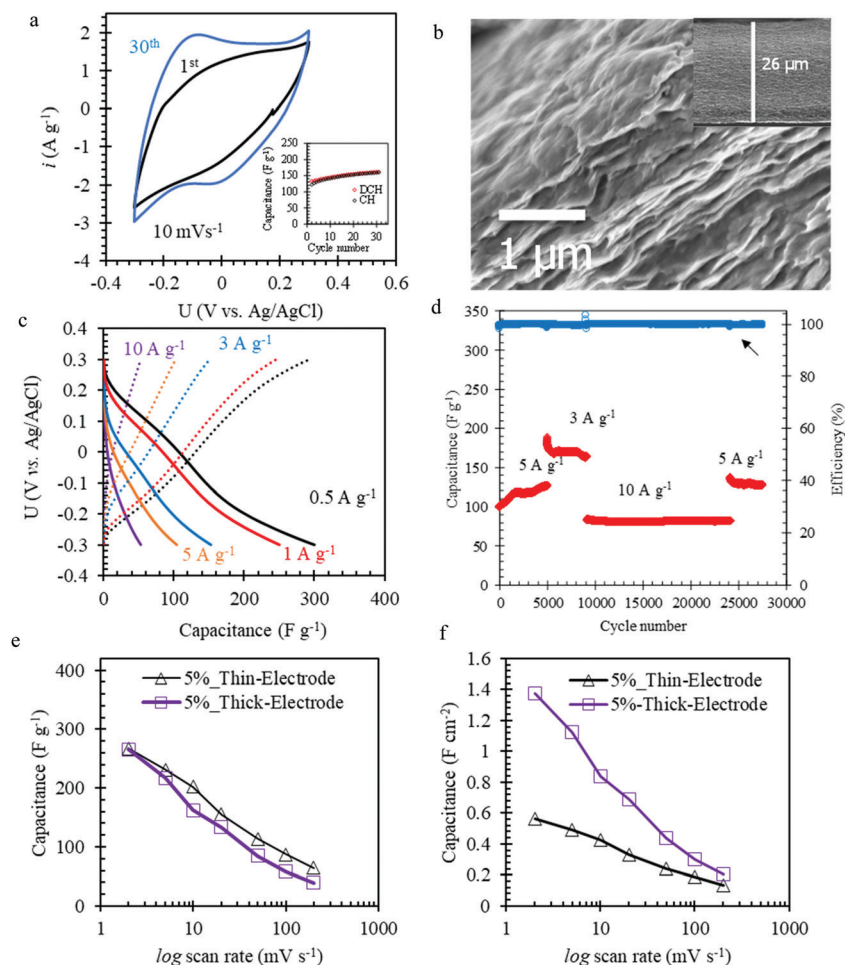
Fig. 4 Electrochemical performance of thick electrodes of $Mo_{1.33}CT_z$–cellulose composite with high MXene loadings (5.2 mg cm^{-2}) in 1 M H_2SO_4 electrolyte solutions: (a) cyclic voltammogram of H-Mo$_x$C-5% Cel electrodes at scan rate of 10 mV s^{-1}. Inset in (a) shows the variation of capacitance with cycle number. (b) Cross-section SEM image of H-Mo$_x$C-5% Cel electrode at high magnification. Inset in (b) shows the thickness of the H-Mo$_x$C-5% Cel electrode. (c) Potential capacitance profiles for H-Mo$_x$C-5% Cel electrodes under applied current densities of 0.5 (black), 1 (red), 3 (blue), 5 (orange), and 10 (violet) A g^{-1}. (d) Variation of discharge capacitance with cycle number for H-Mo$_x$C-5% Cel electrodes at different applied current densities of 3, 5, and 10 A g^{-1}. (e) Variation of the gravimetric discharge capacitances with scan rates for H-Mo$_x$C-5% (violet squares) and L-Mo$_x$C-5% Cel (black triangles) electrodes. (f) Variation of the areal discharge capacitances with scan rates for H-Mo$_x$C-5% (violet squares) and L-Mo$_x$C-5% Cel (black triangles) electrodes.

impedance spectroscopy (EIS) is measured to track the changes in the ion transport and charge transfer resistance (R_{ct}) during the electrochemical cycling of H-Mo$_x$C-5% Cel electrodes. As can be seen from the Nyquist plots, the slope of the straight lines in the low frequency region (Fig. 5c) increases during electrochemical cycling, indicating the increase of the rate of ions transport. Furthermore, the charge transfer resistance (R_{ct}) in the high frequency region (Fig. 5d) decreases upon electrochemical cycling as indicated by the decrease of the semicircle diameter on the Nyquist plots. An equivalent circuit model for the Nyquist plots is shown in Fig. S6c (ESI†).[59–61] Fig. 5a and b show schematic illustrations for the possible ion transport in the pristine MXene and the $Mo_{1.33}CT_z$-cellulose composite, respectively, where the presence of cellulose between the MXene sheets increases the *in-plane* ion transport and hence the accessible capacitance.

Notably, the galvanostatic charge–discharge experiments showed that the discharge capacitance of the H-Mo$_x$C-5% Cel electrodes were about 300, 104, and 53 F g^{-1} at current densities

of 0.5, 5, and 10 A g^{-1}, respectively (see Fig. 4c). These capacitance values were higher than those obtained using thin L-Mo$_x$C-0% Cel electrodes (4.2 µm-thick, mass loadings 1.56 mg cm^{-2}). Likewise, the long-term cycling of the H-Mo$_x$C-5% Cel electrodes at different applied current densities exhibited a stable electrochemical response for 30 000 cycles. It worth mentioning that the amount of cellulose per unit area rather than the cellulose weight percentage is the more crucial factor in determining the long-term cycling of the electrodes. For instance, L-Mo$_x$C-5% Cel (cellulose loading 0.10 mg cm^{-2}) showed a stable behavior for only 8000 cycles (see Fig. S5b, ESI†), although it contained the same weight percentage of cellulose as compared to H-Mo$_x$C-5% Cel (cellulose loading 0.31 mg cm^{-2}).

The variation of gravimetric specific capacitances for electrodes with relatively similar cellulose content (5 wt%) and varying MXene loading (and hence different electrode thickness) is shown in Fig. 4e. As can be seen, at low scan rates the capacitance of the electrodes with high MXene loading (H-Mo$_x$C-5% Cel, thick
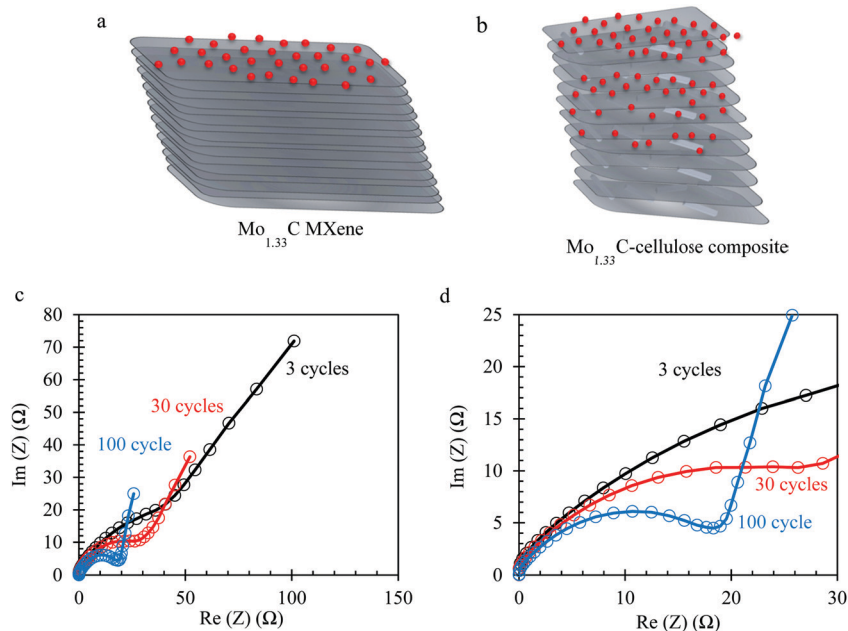
Fig. 5 (a) and (b) Schematic illustration of the ion transport during electrochemical cycling of the $Mo_{1.33}CT_z$ MXene and the $Mo_{1.33}CT_z$–cellulose composite, respectively. The red balls represent the protons of the electrolyte, where the *in-plane* ion transport is hindered in the pristine MXene owing to the restacking of MXene sheets. (c) and (d) Nyquist plots of the H-Mo_xC 5% Cel electrodes collected after 3rd (black), 30th (red) and 100th CV cycles at 10 mV s^{-1}, indicating the decrease in the charge transfer resistance and increase of ions transport upon electrochemical cycling.

electrode) is comparable with that of the electrodes with low loading (L-Mo_xC-5% Cel, thin electrode). However, at higher scan rate the capacitance of H-Mo_xC-5% Cel electrodes was lower than those of L-Mo_xC-5% Cel electrodes. This observation
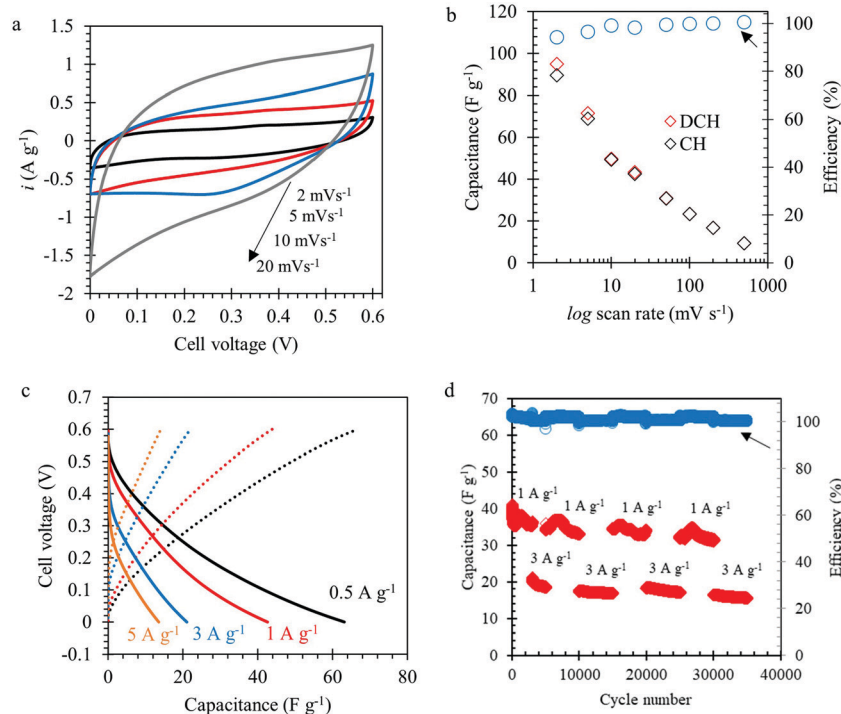
Fig. 6 Electrochemical performance of the symmetric device of $Mo_{1.33}CT_z$–cellulose composite electrodes (L-Mo_xC-25% Cel symmetric device) in 1 M H_2SO_4 solution: (a) cyclic voltammograms of the symmetric device at scan rates of 2, 5, 10 and 20 mV s^{-1}. (b) Variation of the charge–discharge capacitances with scan rates. (c) Potential capacitance profiles for the symmetric device under applied current densities of 0.5 (black), 1 (red), 3 (blue), and 5 (orange) A g^{-1}. (d) Variation of discharge capacitance with cycle number for the symmetric device at applied current densities of 1 and 3 A g^{-1}.

Table 1 Summary of the $Mo_{1.33}CT_z$–cellulose electrodes prepared in this study

Sample	MXene			Cellulose			Film thickness (μm)	Overall electrode mass (4 mm diameter) (μg)
	Volume (Concentration)	(wt%)	Loading (mg cm^{-2})	Mass (mg)	(wt%)	Loading (mg cm^{-2})		
L-Mo$_x$C-0% Cel	25 ml (0.6 mg ml^{-1})	100	1.56	—	—	—	4.2	200
L-Mo$_x$C-5% Cel	25 ml (0.7 mg ml^{-1})	95	1.82	1	5	0.10	4.8	280
L-Mo$_x$C-25% Cel	25 ml (0.6 mg ml^{-1})	75	1.56	5	25	0.52	4.8	240
L-Mo$_x$C-45% Cel	25 ml (0.6 mg ml^{-1})	55	1.56	12	45	1.25	5.9	310
H-Mo$_x$C-0% Cel	50 ml (0.8 mg ml^{-1})	100	4.0	—	—	—	15	500
H-Mo$_x$C-5% Cel	25 ml (2 mg ml^{-1})	95	5.20	3	5	0.31	26	690

can be attributed to a combination of more limited diffusion and an increased iR drop for the H-Mo$_x$C-5% Cel electrodes (26 μm thickness) compared to the L-Mo$_x$C-5% Cel (4.8 μm thickness). However, for a real device the amount of charge stored per unit area is critical. To demonstrate the amount of charge stored per unit area for the low and high loading MXene series, we compared the areal capacitance for L-Mo$_x$C-5% Cel and H-Mo$_x$C-5% Cel electrodes with similar area (about 0.13 cm^{-2}) at different scan rates, shown in Fig. 4f. At low scan rate (2 mV s^{-1}) the H-Mo$_x$C-5% areal capacitance was about 1.4 F cm^{-2}, whereas that of the L-Mo$_x$C-5% was only about 0.6 F cm^{-2}. Therefore, at low scan rate the H-Mo$_x$C-5% electrodes can store a factor 2.3 higher areal charge than that of L-Mo$_x$C-5%. However, at high scan rates (200 mV s^{-1}), the areal capacitance of H-Mo$_x$C-5% ($\sim$202 mF cm^{-2}) is about a factor 1.5 higher than that of L-Mo$_x$C-5% ($\sim$135 mF cm^{-2}). Table S2 (ESI†) summarizes a comparision between the performance of the composite electrodes reported herein and other state-of-the-art electrodes based on Ti and Mo. It can be clearly seen that the presence of the cellulose in the $Mo_{1.33}CT_z$ electrodes efficiently improved the electrochemical performance and increased the life-span as compared to previous reports.

A symmetric device was assembled using L-Mo$_x$C 25% electrodes and was cycled between 0 and 0.6 V in 1 M H$_2$SO$_4$ solution. Fig. 6a shows the CVs of the device at different scan rates. A typical pseudocapacitive behavior was observed, similar to the results obtained using the three-electrode setup (see Fig. 2a and b). The variation of the device capacitance with scan rates (see Fig. 6b) showed that the device capacitance was about 95, 50, 30 and 23 F g^{-1} at scan rates of 2, 10, 50, and 100 mV s^{-1}, respectively. In other words, a capacitance retention of about 25% was obtained when the scan rate was raised from 2 to 100 mV s^{-1}. In addition, the coulombic efficiency was close to 100% at the different rates. Likewise, the constant current measurements (see Fig. 6c) showed that the device capacitance was about 63, 43, 21, and 13 F g^{-1} for an applied current density of 0.5, 1, 3, and 5 A g^{-1}, respectively. Furthermore, the long-term cycling of the symmetric device displayed a promising behavior for 35 000 cycles without a significant capacitance loss (see Fig. 6d).

3. Conclusions

To summarize, we developed a one-step vacuum filtration approach to fabricate $Mo_{1.33}CT_z$–cellulose freestanding composite electrodes

with high MXene loading (5.2 mg cm^{-2}), high areal capacitance (1.4 F cm^{-2}) and 95% capacitance retention over 30 000 cycles. The composite electrodes not only showed superior electrochemical performance in supercapacitors, but also exhibited improved handling and flexibility as compared to the $Mo_{1.33}CT_z$ electrodes without cellulose. The composite electrodes featured a typical layered morphology, with the cellulose crystals providing tunnels between the $Mo_{1.33}CT_z$ nanosheets. Therefore, when the amount of cellulose content was increased from 5 to 45 wt%, the accessible gravimetric specific capacitance was increased. Moreover, the rate performance of the electrodes could be improved by increasing the molarity of the H$_2$SO$_4$ electrolyte solution from 1 to 3, owing to the increased ionic conductivity of the electrolyte.

The electrodes with high MXene loading ($\sim$5.2 mg cm^{-2}) showed a comparable gravimetric specific capacitance to that of low MXene loading (1.56 mg cm^{-2}). Furthermore, the electrodes with high loading could deliver an areal capacitance up to 1.4 F cm^{-2} as compared to that of electrodes with low loading of only about 0.6 F cm^{-2}. The presence of cellulose was found to be crucial for opening the structure of the thick electrode during electrochemical cycling. In addition, the amount of cellulose per electrode area rather than the percentage of the cellulose in the electrodes was found to play a crucial role in the long-term cycling of the electrodes. A symmetric device based on $Mo_{1.33}CT_z$–cellulose freestanding electrodes was tested in 1 M H$_2$SO$_4$ solution, and delivered a specific capacitance of 97 and 23 F g^{-1} at scan rates of 2 and 100 mV s^{-1}, respectively. The device also showed a promising lifespan for about 35 000 cycles. Altogether, the results suggest that use of $Mo_{1.33}CT_z$–cellulose composite electrodes facilitates a pathway for reaching the requirements needed for potential applications. To further explore the full potential of these $Mo_{1.33}CT_z$–cellulose composite electrodes, studies focusing on modifying the morphology of the pristine cellulose are motivated, such as investigating the use of cellulose nanofibers or nanocrystals. It should also be noted that the electrodes porosity can be improved by using freeze drying directly after the vacuum filtration.

4. Experimental

4.1 Synthesis of the $Mo_{1.33}CT_z$ MXene

The precursor $(Mo_{2/3}Sc_{1/3})_2AlC$ was synthetized by mixing stoichiometric ratios of Mo (99.99%, Sigma-Aldrich), Al (99.8% Alfa Aesar), Sc (99.99%, Standford Advanced Material), and graphite

(99.999% Alfa Aesar) in an agate mortar. The mixture was then placed in an alumina crucible and heated in an alumina tube furnace up to 1500 °C for 600 h under flowing argon. After cooling, a lightly sintered sample was obtained which was crushed and sieved through a 450 mesh sieve (particle size < 32 μm).

To produced $Mo_{1.33}CT_z$ (MXene), 1 gram of $(Mo_{2/3}Sc_{1/3})_2AlC$ was slowly added to a Teflon bottle containing 20 ml of 48% HF (Sigma-Aldrich) which was kept for 30 h at RT while stirring. After etching, the $Mo_{1.33}CT_z$ (MXene) was washed three times with 1 M HCl to get rid of any ScF_3 leftovers. This was done by adding 50 ml of 1 M HCl to the etched powder, hand-shaking for 1 min (~ 2 shakes per second), then centrifuging for 1 min at 5500 rpm, and then the supernatant was decanted. Afterwards, the $Mo_{1.33}CT_z$ (MXene) was washed with deionized water (DI) several times until the pH was above 5. Then the $Mo_{1.33}CT_z$ (MXene) powder was delaminated by adding 10 ml of 40% tetra-butyl ammonium hydroxide (TBAOH), and this mixture was stirred for 1 h at RT. The TBAOH washing was done by first adding 50 ml of 95% ethanol, followed by hand-shaking for 1 min (~ 2 shakes per second), then centrifuging at 5500 rpm for 5 min, after which the supernatant was decanted. To remove the ethanol, 50 ml of DI water was slowly added not to agitate the powder and cause spontaneous delamination, and then decanted; this process was repeated three times. Afterwards, 50 ml of deaerated DI water was added to the washed MXene and then sonicated for 1 h while bubbling Ar. After sonication, the mixture was centrifuged for 1 h at 3000 rpm, and the supernatant (which contains a colloidal suspension of single flakes) was then used in the synthesis of $Mo_{1.33}CT_z$–cellulose composite electrodes.

4.2 Synthesis of the $Mo_{1.33}CT_z$–cellulose composite electrodes

The $Mo_{1.33}CT_z$–cellulose electrodes were fabricated using a single step protocol. In a typical experiment, a given amount of the cellulose (1–12 mg) was dispersed inside the as prepared $Mo_{1.33}CT_z$ aqueous suspension (25–50 ml of concentration 0.6–2 mg ml^{-1}) using sonication for about 20–30 minutes. The $Mo_{1.33}CT_z$–cellulose dispersion was then vacuum filtrated through a Celgard 3501 membrane. After filtration the film was allowed to dry in air for 20 minutes, and was then peeled off the Celgard membrane, and placed in an Ar-filled glove box until further use. So far, we prepared two series of samples in which the amount of MXene was fixed and the amount of cellulose was varied. The first series with a relatively low loading of MXene was nominated L-Mo$_x$C-% Cel, where (% Cel) refers to weight percentage of cellulose inside the electrodes. Likewise, the second series with a relatively high loading of MXene was nominated H-Mo$_x$C-% Cel. The composition, film thickness, cellulose content, and electrode loading for the samples used in this study is summarized in Table 1.

4.3 Material characterization and electrochemical measurements

The morphology and thickness of the different electrodes were evaluated using a Scanning Electron Microscope (SEM, LEO 1550 Gemini). X-Ray diffraction (XRD) measurements were done using a PANalytical diffractometer mounted with Cu K$_\alpha$ radiation source ($\lambda = 1.54$ Å, step size 0.0084°, time per step 20 s).

All electrochemical analysis was done using a stainless-steel Swagelok cell. Circular pieces of gold foil were used as a current collector, a piece of Celgard 3501 was used as the separator, and about 500 μl of 1 M or 3 M H_2SO_4 solution was used as the electrolyte. For three-electrode measurements, a circular electrode of activated carbon (YP-50, Kuraray, Japan) was used as the counter electrode, whereas an Ag/AgCl (3.5 M KCl) was used as a reference electrode. The pristine $Mo_{1.33}CT_z$ and $Mo_{1.33}CT_z$–cellulose composite electrodes were used as the working electrodes. The overall working electrode mass varied between 200 and 690 μg and the capacitances were normalized with respect to the mass of $Mo_{1.33}CT_z$ active material. The electrodes had a diameter of about 4.0 mm unless otherwise noted; a few experiments were done with electrodes of a diameter of 6.4 mm. Cyclic voltammetry and galvanostatic charge–discharge techniques were used to study the electrochemical behavior of the electrodes in a potential window between −0.3 and 0.3 V vs. Ag/AgCl (3.5 M KCl). The electrochemical impedance spectroscopy (EIS) was collected in the frequency range from 100 mHz to 200 kHz using an amplitude of 10 mV. Likewise, the two electrode symmetric device experiments were performed using a couple of symmetric circular (4.0 mm, diameter) electrodes. The overall mass of each electrode was about 240 μg. Cyclic voltammetry and constant current techniques were used to explore the electrochemical performances of the symmetric devices and the cell voltage was varied between 0 and 0.6 V.

Conflicts of interest

There are no conflicts to declare.

Acknowledgements

References

1 C. Tan, X. Cao, X.-J. Wu, Q. He, J. Yang, X. Zhang, J. Chen, W. Zhao, S. Han, G.-H. Nam, M. Sindoro and H. Zhang, *Chem. Rev.*, 2017, **117**, 6225–6331.

2 H. Zhao, Y. Zhu, F. Li, R. Hao, S. Wang and L. Guo, *Angew. Chem., Int. Ed.*, 2017, **56**, 8766–8770.

3 A. S. Etman, L. Wang, K. Edström, L. Nyholm and J. Sun, *Adv. Funct. Mater.*, 2019, **29**, 1806699.

4 A. S. Etman, A. K. Inge, X. Jiaru, R. Younesi, K. Edström and J. Sun, *Electrochim. Acta*, 2017, **252**, 254–260.

5 A. S. Etman, PhD thesis, Stockholm University, 2019.

6 A. S. Etman, A. J. Pell, P. Svedlindh, N. Hedin, X. Zou, J. Sun and D. Bernin, *ACS Omega*, 2019, **4**, 10899–10905.

7 W. Choi, N. Choudhary, G. H. Han, J. Park, D. Akinwande and Y. H. Lee, *Mater. Today*, 2017, **20**, 116–130.

8 M. Chhowalla, H. S. Shin, G. Eda, L.-J. Li, K. P. Loh and H. Zhang, *Nat. Chem.*, 2013, **5**, 263–275.

9 M. Naguib, M. Kurtoglu, V. Presser, J. Lu, J. Niu, M. Heon, L. Hultman, Y. Gogotsi and M. W. Barsoum, *Adv. Mater.*, 2011, **23**, 4248–4253.

10 M. Naguib, O. Mashtalir, J. Carle, V. Presser, J. Lu, L. Hultman, Y. Gogotsi and M. W. Barsoum, *ACS Nano*, 2012, **6**, 1322–1331.

11 X. Xiao, H. Wang, P. Urbankowski and Y. Gogotsi, *Chem. Soc. Rev.*, 2018, **47**, 8744–8765.

12 J. Halim, K. M. Cook, M. Naguib, P. Eklund, Y. Gogotsi, J. Rosen and M. W. Barsoum, *Appl. Surf. Sci.*, 2016, **362**, 406–417.

13 R. Meshkian, L.-Å. Näslund, J. Halim, J. Lu, M. W. Barsoum and J. Rosen, *Scr. Mater.*, 2015, **108**, 147–150.

14 J. Halim, S. Kota, M. R. Lukatskaya, M. Naguib, M.-Q. Zhao, E. J. Moon, J. Pitock, J. Nanda, S. J. May, Y. Gogotsi and M. W. Barsoum, *Adv. Funct. Mater.*, 2016, **26**, 3118–3127.

15 M. Alhabeb, K. Maleski, T. S. Mathis, A Sarycheva, C. B. Hatter, S. Uzun, A. Levitt and Y. Gogotsi, *Angew. Chem.*, 2018, **57**(19), 5444–5448.

16 M. Alhabeb, K. Maleski, B. Anasori, P. Lelyukh, L. Clark, S. Sin and Y. Gogotsi, *Chem. Mater.*, 2017, **29**, 7633–7644.

17 Y. Wang, X. Wang, X. Li, Y. Bai, H. Xiao, Y. Liu, R. Liu and G. Yuan, *Adv. Funct. Mater.*, 2019, **29**, 1900326.

18 E. Pomerantseva, F. Bonaccorso, X. Feng, Y. Cui and Y. Gogotsi, *Science*, 2019, **366**, eaan8285.

19 J. K. El-Demellawi, S. Lopatin, J. Yin, O. F. Mohammed and H. N. Alshareef, *ACS Nano*, 2018, **12**, 8485–8493.

20 K. Chaudhuri, M. Alhabeb, Z. Wang, V. M. Shalaev, Y. Gogotsi and A. Boltasseva, *ACS Photonics*, 2018, **5**, 1115–1122.

21 Z. Chen, Y. Hu, H. Zhuo, L. Liu, S. Jing, L. Zhong, X. Peng and R. Sun, *Chem. Mater.*, 2019, **31**, 3301–3312.

22 Z. W. Seh, K. D. Fredrickson, B. Anasori, J. Kibsgaard, A. L. Strickler, M. R. Lukatskaya, Y. Gogotsi, T. F. Jaramillo and A. Vojvodic, *ACS Energy Lett.*, 2016, **1**, 589–594.

23 K. R. G. Lim, A. D. Handoko, L. R. Johnson, X. Meng, M. Lin, G. S. Subramanian, B. Anasori, Y. Gogotsi, A. Vojvodic and Z. W. Seh, *ACS Nano*, 2020, **14**, 16140–16155.

24 J. Pang, R. G. Mendes, A. Bachmatiuk, L. Zhao, H. Q. Ta, T. Gemming, H. Liu, Z. Liu and M. H. Rummeli, *Chem. Soc. Rev.*, 2019, **48**, 72–133.

25 Y. Yuan, H. Li, L. Wang, L. Zhang, D. Shi, Y. Hong and J. Sun, *ACS Sustainable Chem. Eng.*, 2019, **7**, 4266–4273.

26 A. D. Handoko, K. D. Fredrickson, B. Anasori, K. W. Convey, L. R. Johnson, Y. Gogotsi, A. Vojvodic and Z. W. Seh, *ACS Appl. Energy Mater.*, 2018, **1**, 173–180.

27 A. D. Handoko, H. Chen, Y. Lum, Q. Zhang, B. Anasori and Z. W. Seh, *iScience*, 2020, **23**, 101181.

28 A. D. Handoko, S. N. Steinmann and Z. W. Seh, *Nanoscale Horiz.*, 2019, **4**, 809–827.

29 K. R. G. Lim, A. D. Handoko, S. K. Nemani, B. Wyatt, H.-Y. Jiang, J. Tang, B. Anasori and Z. W. Seh, *ACS Nano*, 2020, **14**, 10834–10864.

30 K. Rasool, R. P. Pandey, P. A. Rasheed, S. Buczek, Y. Gogotsi and K. A. Mahmoud, *Mater. Today*, 2019, **30**, 80–102.

31 D. Pang, M. Alhabeb, X. Mu, Y. Dall'Agnese, Y. Gogotsi and Y. Gao, *Nano Lett.*, 2019, **19**, 7443–7448.

32 H. Chen, Y. Wen, Y. Qi, Q. Zhao, L. Qu and C. Li, *Adv. Funct. Mater.*, 2020, **30**, 1906996.

33 S. Niu, Z. Wang, M. Yu, M. Yu, L. Xiu, S. Wang, X. Wu and J. Qiu, *ACS Nano*, 2018, **12**, 3928–3937.

34 Z. Ma, X. Zhou, W. Deng, D. Lei and Z. Liu, *ACS Appl. Mater. Interfaces*, 2018, **10**, 3634–3643.

35 X. Tang, X. Guo, W. Wu and G. Wang, *Adv. Energy Mater.*, 2018, **8**, 1–21.

36 Y. Han, Y. Ge, Y. Chao, C. Wang and G. G. Wallace, *J. Energy Chem.*, 2018, **27**, 57–72.

37 H. Shao, Z. Lin, K. Xu, P. Taberna and P. Simon, *Energy Storage Mater.*, 2019, **18**, 456–461.

38 B. Anasori, M. R. Lukatskaya and Y. Gogotsi, *Nat. Rev. Mater.*, 2017, **2**, 16098.

39 M. R. Lukatskaya, S. Kota, Z. Lin, M. Zhao, N. Shpigel, M. D. Levi, J. Halim, P. Taberna, M. W. Barsoum, P. Simon and Y. Gogotsi, *Nat. Energy*, 2017, **2**, 17105.

40 M. Ghidiu, M. R. Lukatskaya, M.-Q. Zhao, Y. Gogotsi and M. W. Barsoum, *Nature*, 2014, **516**, 78–81.

41 J. Shojaeiarani, D. Bajwa and A. Shirzadifar, *Carbohydr. Polym.*, 2019, **216**, 247–259.

42 J. Wang, J. Tavakoli and Y. Tang, *Carbohydr. Polym.*, 2019, **219**, 63–76.

43 O. Nechyporchuk, M. N. Belgacem and J. Bras, *Ind. Crops Prod.*, 2016, **93**, 2–25.

44 L. Nyholm, G. Nyström, A. Mihranyan and M. Strømme, *Adv. Mater.*, 2011, **23**, 3751–3769.

45 A. S. Etman, Z. Wang, A. El Ghazaly, J. Sun, L. Nyholm and J. Rosen, *ChemSusChem*, 2019, **12**, 5157–5163.

46 A. S. Etman, Z. Wang, Y. Yuan, L. Nyholm and J. Rosen, *Energy Technol.*, 2020, **8**, 2000731.

47 W. Cao, C. Ma, D. Mao, J. Zhang, M. Ma and F. Chen, *Adv. Funct. Mater.*, 2019, **29**, 1905898.

48 S. Jiao, A. Zhou, M. Wu and H. Hu, *Adv. Sci.*, 2019, **6**, 1900529.

49 W. Tian, A. VahidMohammadi, M. S. Reid, Z. Wang, L. Ouyang, J. Erlandsson, T. Pettersson, L. Wågberg, M. Beidaghi and M. M. Hamedi, *Adv. Mater.*, 2019, **31**, 1902977.

50 Q. Tao, M. Dahlqvist, J. Lu, S. Kota, R. Meshkian, J. Halim, J. Palisaitis, L. Hultman, M. W. W. Barsoum, P. O. Å. O. Å. Persson and J. Rosen, *Nat. Commun.*, 2017, **8**, 14949.

51 L. Qin, Q. Tao, A. El Ghazaly, J. Fernandez-Rodriguez, P. O. Å. Persson, J. Rosen and F. Zhang, *Adv. Funct. Mater.*, 2018, **28**, 1703808.

52 M. Gubitosi, H. Duarte, L. Gentile, U. Olsson and B. Medronho, *Biomacromolecules*, 2016, **17**, 2873–2881.

53 W. Wei, X. Wei, G. Gou, M. Jiang, X. Xu, Y. Wang, D. Hui and Z. Zhou, *RSC Adv.*, 2015, **5**, 39080–39083.

54 L. Alves, B. Medronho, F. E. Antunes, D. Topgaard and B. Lindman, *Cellulose*, 2016, **23**, 247–258.

55 M. A. Behrens, J. A. Holdaway, P. Nosrati and U. Olsson, *RSC Adv.*, 2016, **6**, 30199–30204.

56 B. Swensson, A. Larsson and M. Hasani, *Cellulose*, 2020, **27**, 101–112.

57 T. S. Mathis, N. Kurra, X. Wang, D. Pinto, P. Simon and Y. Gogotsi, *Adv. Energy Mater.*, 2019, **9**, 1902007.

58 A. Bard and L. Faulkner, *Electrochemical Methods: Fundamentals and Applications*, John Wiley & Sons, Inc., 2001.

59 B. E. Conway, *Electrochemical Supercapacitors: Scientific Fundamentals and Technological Applications*, Springer US, Boston, MA, 1999.

60 N. Sun, Z. Guan, Q. Zhu, B. Anasori, Y. Gogotsi and B. Xu, *Nano-Micro Lett.*, 2020, **12**, 89.

61 J. Kong, H. Yang, X. Guo, S. Yang, Z. Huang, X. Lu, Z. Bo, J. Yan, K. Cen and K. K. Ostrikov, *ACS Energy Lett.*, 2020, **5**, 2266–2274.